N-(Methoxycarbonyl)-*N*-methyl-1-methoxybenzylamine (5e): colorless oil; ^{1}H NMR ($CDCl_3$) δ 2.56 and 2.59 (s, 3 H), 3.43 (s, 3 H), 3.80 and 3.82 (s, 3 H), 6.24 and 6.43 (s, 1 H), 7.27-7.39 (m, 5 H); ^{13}C NMR ($CDCl_3$, at -55 °C) δ 27.15 and 27.23, 53.03 and 53.27, 55.22 and 55.31, 85.90 and 86.07, 125.82 and 125.91, 127.98 and 128.07, 128.26 and 128.29, 128.66 and 128.99, 137.42 and 137.57, 157.14 and 157.87; IR (CCl_4) 2950, 1715, 1455, 1395, 1330, 1155, 1100, 990 cm^{-1}; HRMS calcd for $C_{11}H_{15}NO_3$ m/z 209.1052, found for m/z 209.1049.

N-(Methoxycarbonyl)-*N*-methyl-1-methoxy-*p*-methoxybenzylamine (5f): colorless oil; ^{1}H NMR ($CDCl_3$) δ 2.55 and 2.58 (s, 3 H), 3.40 (s, 3 H), 3.80 (s, 6 H), 6.18 and 6.36 (s, 1 H), 6.87 (d, J = 8 Hz, 2 H), 7.23-7.32 (m, 2 H); ^{13}C NMR ($CDCl_3$) δ 26.95, 52.78, 55.25 and 55.35, 86.39, 113.62, 127.37, 130.30, 159.34; IR (CCl_4) 2995, 2950, 2830, 1705, 1615, 1510, 1450, 1325, 1250, 1175, 1150, 1090, 1040, 985 cm^{-1}; HRMS calcd for $C_{12}H_{17}NO_3$ m/z 239.1158, found for m/z 239.1161.

Synthesis of Chiral α-Alkoxycarbamates. Synthesis of **5h** is representative. In a 200-mL flask under Ar were placed 8-phenylmenthol (5.59 g, 24.0 mmol), benzene (150 mL), and trichloromethyl chloroformate (TCF) (6.0 mL, 50 mmol). The mixture was refluxed at 100 °C for 13 h and then stirred at room temperature for 18 h. Pyridine (2.2 mL, 27.2 mmol) was added. Complete consumption of the starting materials was confirmed by TLC analysis. The solvent was removed under reduced pressure, and then benzene was added. The mixture was filtered through Celite under reduced pressure. Removal of solvent gave crude 8-phenylmenthyl chloroformate, which was immediately transferred to a 200-mL flask under Ar and dissolved in 60 mL of CH_2Cl_2. A CH_2Cl_2 (10 mL) solution of *N*-(*p*-methylbenzylidene)methylamine (3.21 g, 24.1 mmol) was prepared in a 50-mL flask under Ar, and the solution was transferred to the 200-mL flask cooled to 0 °C through a double-ended needle. Stirring was continued for 3 h at room temperature, and the flask was cooled to 0 °C. Triethylamine (4.0 mL, 28.7 mmol) and then methanol (2.0 mL, 49.4 mmol) were added. Stirring was continued overnight at room temperature. A similar isolation procedure as mentioned above was used. Crude yellow oil (9.59 g) was obtained. Purification with a flash silica gel column chromatography using hexane-EtOAc (30:1) as an eluant gave a colorless oil (5.53 g, 54%).

N-[(-)-Menthoxycarbonyl]-*N*-methyl-1-methoxy-*p*-methylbenzylamine (5g): colorless oil; ^{1}H NMR ($CDCl_3$, at -55 °C) δ 0.7-2.3 (m, 15 H), 0.93 (br s, 3 H), 2.37 (s, 3 H), 2.56 and 2.57 and 2.61 (s, 3 H), 3.42 and 3.44 (s, 3 H), 4.70-4.90 (m, 1 H), 6.30 and 6.33 and 6.45 and 6.46 (s, 1 H), 7.19-7.32 (m, 4 H); ^{13}C NMR ($CDCl_3$) δ 16.21, 16.61, 20.78, 21.07, 22.04, 23.30, 23.80, 26.65, 26.97, 31.45, 34.38, 41.57, 47.49, 55.04, 75.51, 86.39, 126.02, 128.92, 130.09, 135.40, 137.52; IR (CCl_4) 2970, 2940, 2880, 1700, 1445, 1400, 1330, 1310, 1165, 1150, 1090, 980 cm^{-1}; HRMS calcd for $C_{21}H_{33}NO_3$ m/z 347.2461, found for m/z 347.2465.

N-[(-)-(8-Phenylmenthoxy)carbonyl]-*N*-methyl-1-methoxy-*p*-methylbenzylamine (major isomer) (5h): colorless oil; ^{1}H NMR ($CDCl_3$) δ 0.85-2.15 (m, 8 H), 0.89 (d, J = 7 Hz, 3 H), 1.23 (s, 3 H), 1.35 (s, 3 H), 1.88 and 2.62 (s, 3 H), 2.37 (s, 3 H), 3.33 (s, 3 H), 4.86 (dt, J = 4 Hz, J = 10 Hz, 1 H), 6.10 and 6.33 (s, 1 H), 6.99 (m, 1 H), 7.09-7.28 (m, 8 H); ^{13}C NMR ($CDCl_3$) δ 21.16, 21.83, 24.82, 26.21, 26.69, 28.29, 31.35, 34.67, 39.65, 42.41, 50.55, 55.19, 75.32, 86.23, 124.87, 125.19, 126.22, 127.93, 128.76, 135.30, 137.48, 152.22, 156.55; IR (CCl_4) 2960, 2930, 1695, 1445, 1395, 1320, 1155, 1090, 980 cm^{-1}. Anal. Calcd for $C_{27}H_{37}NO_3$: C, 76.56; H, 8.80; N, 3.31. Found for C, 76.42; H, 8.93; N, 3.33.

N-[(-)-(8-Phenylmenthoxy)carbonyl]-*N*-methyl-1-methoxy-*p*-methylbenzylamine (minor isomer) (5h): colorless oil; ^{1}H NMR ($CDCl_3$) δ 0.86-2.10 (m, 8 H), 0.89 (d, J = 6 Hz, 3 H), 1.24 (s, 3 H), 1.38 (s, 3 H), 1.93 and 2.58 (s, 3 H), 2.30 and 2.32 (s, 3 H), 3.36 and 3.40 (s, 3 H), 4.87 (dt, J = 4 Hz, J = 10 Hz, 1 H), 5.91 and 6.34 (s, 1 H), 7.09-7.33 (m, 9 H).

NMR Measurement. The α-alkoxycarbamates **5** (0.5 ~ 0.1 mmol) were placed in a 5-mm NMR tube with a septum cap under Ar atmosphere. $CDCl_3$ (0.65 mL) and 0.05 mL of $CDCl_3$ containing 1% TMS were added. The solvent was dried with molecular sieves (4A) prior to use. The tube was cooled to an appropriate temperature, and then the Lewis acid was added by a microsyringe. The tube was transferred rapidly to a NMR probe which was cooled to -55 °C.

Supplementary Material Available: ^{1}H NMR spectra of **5a** + TMSOTf and **5c** + TMSOTf (Figure 3a,b) and **5g** and **5g** + BF_3 (Figure 7a,b) (2 pages). Ordering information is given on any current masthead page.

NMR Imaging of Anisotropic Solid-State Chemical Reactions Using Multiple-Pulse Line-Narrowing Techniques and ^{1}H T_1 Weighting

Leslie G. Butler,*,†,[1a] David G. Cory,‡,[1b] Kerry M. Dooley,[1c] Joel B. Miller,[1b] and Allen N. Garroway*,[1b]

Contribution from Code 6122, Chemistry Division, Naval Research Laboratory, Washington, D.C. 20375-5000, Department of Chemistry, Louisiana State University, Baton Rouge, Louisiana 70803-1804, and Department of Chemical Engineering, Louisiana State University, Baton Rouge, Louisiana 70803-7303. *Received May 20, 1991*

Abstract: The reactions of substituted benzoic acid crystals and powders with ammonia gas have been monitored using solid-state ^{1}H NMR imaging techniques. The reactions are inherently (crystal) or by design (powder) spatially anisotropic: For a crystal of 4-bromobenzoic acid, the expected reaction anisotropy was not seen, either optically or with ^{1}H NMR imaging, most likely due to poor crystal quality or an unexpected crystal morphology. Nevertheless, some anisotropy in the reaction was observed and the extent of reaction was obtained from the NMR images. For a deep bed of powdered toluic acid, an anisotropic reaction profile is found. The reaction of the more exposed top layers of the bed is rapid whereas there is a delay in the reaction of the bottom layers associated with the rate of diffusion of ammonia into the bed. The apparent reaction rate constant, k = 5 (2) × 10^{-4} mol^{-1} m^3 s^{-1}, and the effective diffusivity, D_e = 1.0 (4) × 10^{-5} m^2 s^{-1}, were obtained from a fit to a simultaneous diffusion with reaction model for a slab. This work is the first application of ^{1}H NMR imaging, using multiple-pulse line-narrowing techniques, for monitoring a chemical reaction. For this work, the special advantage of line narrowing is that the images are weighted not by the ^{1}H T_2 but rather by the T_1 relaxation time. Thus, for the materials studied herein, selection of an appropriate relaxation time in the NMR experiment enables observation of either the reaction product or the total sample.

Introduction

Anisotropic chemical reactions are common. Reactions at interfaces are necessarily anisotropic, for example, the reaction of oxygen with a silicon surface.[2] However, it is difficult to visualize the progress of such anisotropic chemical reactions.

* Author to whom correspondence should be addressed.
† Fellow of the Alfred P. Sloan Foundation (1989-1991).
‡ Present address: Bruker Instruments, Inc., Manning Park, Billerica, MA 01821.

(1) (a) Department of Chemistry, Louisiana State University. (b) Naval Research Laboratory. (c) Department of Chemical Engineering, Louisiana State University.
(2) Deal, B. E. Grove, A. S. *J. Appl. Phys.* **1965**, *36*, 3770-8.

0002-7863/92/1514-125$03.00/0

Herein, we report the monitoring of an anisotropic acid–base reaction in two different physical configurations using a recently developed solid-state ^1H line-narrowing pulse sequence[3] applied to NMR imaging.

NMR imaging of solids is a technique that can be divided into two areas, depending upon the characteristics of the sample.[4-8] For "soft" solids, the presence of local, rapid molecular motions reduces homonuclear dipolar coupling and averages anisotropic chemical shielding. Thus, the natural line width is narrow (long T_2) and it is relatively easy to encode spatial information with a magnetic field gradient. However, in "rigid" solids there is an absence of local, rapid molecular motions. Therefore, homonuclear dipolar coupling and anisotropic chemical shielding contribute to a large line width, and it becomes exceedingly difficult to encode spatial information within the time allowed by the short T_2. For protons, one solution is to employ multiple-pulse ^1H NMR techniques to diminish either homonuclear dipolar coupling or both homonuclear dipolar coupling and chemical shielding interactions, thus artificially narrowing the resonance and increasing the effective T_2.[9-11] Mansfield and Grannell used a ^1H line-narrowing technique to obtain 1D images of solids.[12] Miller and Garroway,[13] and separately, Cory and Veeman,[14] have addressed the question of when line-narrowing techniques are advantageous in imaging solids. NMR images with multiple pulse line narrowing have been acquired for several different proton-containing solids. The technique of 2D Fourier imaging with MREV-8 line narrowing during evolution periods was used for a rubber/adamantane phantom.[15] Sculptured rubber and Teflon phantoms have been imaged with a sinusoidally driven magnetic field gradient in a multiple-pulse sequence.[16] A 6.4 mm diameter phantom of poly(methyl methacrylate) was imaged at a resolution of about 100 μm using a line-narrowing pulse sequences with interleaved gradient pulses[17] of alternating polarity.[18,19] Techniques for NMR imaging of solids in inhomogeneous rf fields have also been devised.[20] A 48-pulse sequence, CMG-48,[21] has been developed and used to image pressure-crystallized polyethylene with a resolution of 300 μm.[3] In summary, quite good results have been obtained, though the sample dimensions must be small enough to be completely contained within the high-intensity region of the rf coil.

There has been relatively little application of NMR imaging to the study of chemistry. One-dimensional ^{19}F NMR images were obtained while following the intercalation of AsF_5 into graphite; here, the short rotational correlation time for AsF_5 diminishes dipolar coupling in the ^{19}F spin system.[22] Oscillating chemical reactions[23,24] in fluid solution have been imaged in two dimensions; images of the Belousov–Zhabotinskii reaction were acquired at 20-s intervals.[25,26] The swelling of a polystyrene bar by CCl_4 was monitored with 1D ^1H NMR imaging; the image was obtained with T_1 weighting, though by the application of very large magnetic field gradients.[27] NMR imaging of diffusion processes in polymers has been studied.[28-31] NMR imaging of quadrupolar nuclei has been used to monitor temperature gradients[32] and impact-created defect sites.[33] The setting of epoxy resins to create a rigid solid has been followed using line-narrowing techniques[34] while the initial phases of the polymerization of methyl methacrylate have been followed with two- and three-dimensional NMR imaging of the liquid phase.[35]

The reactions of molecular single crystals can exhibit clear anisotropy. For example, the reaction of crystals of 4-chlorobenzoic acid with ammonia gas to form ammonium 4-chlorobenzoate is visibly anisotropic.[36] The crystal faces with an exposed carboxylic group react faster than does the (100) face, which has an array of C–Cl units on the surface that acts to protect the carboxylic function from reaction. Many other anisotropic gas–solid reactions with ammonia have been observed.[37-40] Gases other than ammonia have been used: (+)-1-phenylethylamine,[41,42] (±)-2-butanamine,[43] methylamine,[42] and aniline.[42]

Herein, two separate sets of experiments are described. First, a crystal of 4-bromobenzoic acid is imaged in two dimensions by the use of a recently developed line-narrowing sequence. Because of the relatively small size of the crystal, the signal acquisition portion of the pulse sequence[3] has been modified, as indicated below, so as to increase the signal-to-noise ratio. The crystal is then exposed to ammonia gas and the progress of the reaction is monitored. Unfortunately, the NMR imaging results show that the crystal is of poor quality as reactions are observed across the face of the crystal. Nevertheless, the experiment is successful in that NMR imaging is used to follow the chemical reaction. In the second experiment, a bed of powdered toluic acid is imaged

(3) Cory, D. G.; Miller, J. B.; Garroway, A. N. *J. Magn. Reson.* **1990**, *90*, 205–13.
(4) Mansfield, P.; Morris, P. G. NMR Imaging in Biomedicine. *Adv. Magn. Reson.* **1982**, *Suppl. 2*.
(5) Morris, P. G. *Nuclear Magnetic Resonance Imaging in Medicine and Biology*; Clarendon Press: Oxford, 1986.
(6) Ernst, R. R.; Bodenhausen, G.; Wokaun, A. *Principles of Nuclear Magnetic Resonance in One and Two Dimensions*; Oxford University Press: Oxford, 1987.
(7) Listerud, J. M.; Sinton, S. W.; Drobny, G. P. *Anal. Chem.* **1989**, *61*, 23A–41A.
(8) Cory, D. G. *Annu. Rep. NMR Spectrosc.* In press.
(9) Waugh, J. S.; Wang, C. H.; Huber, L. M.; Vold, R. l. *J. Chem. Phys.* **1968**, *48*, 662–70.
(10) Garroway, A. N.; Mansfield, P.; Stalker, D. C. *Phys. Rev. B* **1975**, *11*, 121–38.
(11) Haeberlen, U. *High Resolution NMR in Solids: Selective Averaging*; Academic Press: New York, 1976.
(12) Mansfield, P.; Grannell, P. K. *Phys. Rev. B* **1975**, *12*, 3618–34.
(13) Miller, J. B.; Garroway, A. N. *J. Magn. Reson.* **1989**, *82*, 529–38.
(14) Cory, D. G.; Veeman, W. S. *J. Magn. Reson.* **1989**, *84*, 392–7.
(15) Chingas, G. C.; Miller, J. B.; Garroway, A. N. *J. Magn. Reson.* **1986**, *66*, 530–5.
(16) McDonald, P. J.; Tokarczuk, P. F. *J. Phys. E; Sci. Instrum.* **1989**, *22*, 948–51.
(17) Miller, J. B.; Cory, D. G.; Garroway, A. N. *Chem. Phys. Lett.* **1989**, *164*, 1–4.
(18) Cory, D. G.; Miller, J. B.; Turner, R.; Garroway, A. N. *Mol. Phys.* **1990**, *70*, 331–45.
(19) Miller, J. B.; Cory, D. G.; Garroway, A. N. *Phil. Trans. R. Soc. A* **1990**, *333*, 413–26.
(20) Miller, J. B.; Garroway, A. N. *J. Magn. Reson.* **1989**, *85*, 432–37.
(21) Initials of authors who developed the 48-pulse line-narrowing sequence. See ref 3.
(22) Chingas, G. C.; Milliken, J.; Resing, H. A.; Tsang, T. *Synth. Met.* **1985**, *12*, 131–6.
(23) Scott, S. K. *Acc. Chem. Res.* **1987**, *20*, 186–91.
(24) Ra'bai, G.; Orba'n, M.; Epstein, I. R. *Acc. Chem. Res.* **1990**, *23*, 258–63.
(25) Armstrong, R. L.; Tzalmona, A.; Menzinger, M.; Cross, A.; Lemaire, C. *Abstracts of the XXV Congress Ampere*, Stuttgart, Germany, 1990; pp 94–5.
(26) Tzalmona, A.; Armstrong, R. L.; Menzinger, M.; Cross, A.; Lemaire, C. *Chem. Phys. Lett.* **1990**, *174*, 199–202.
(27) Corti, M.; Borsa, F.; Rigamonti, A. *J. Magn. Reson.* **1988**, *79*, 21–7.
(28) Weisenberger, L. A.; Koenig, J. L. *Macromolecules* **1990**, *23*, 2454–9.
(29) Weisenberger, L. A.; Koenig, J. L. *Macromolecules* **1990**, *23*, 2445–53.
(30) Webb, A. G.; Hall, L. D. *Polym. Commun.* **1990**, *31*, 422–5.
(31) Webb, A. G.; Hall, L. D. *Polym. Commun.* **1990**, *31*, 425–7.
(32) Suits, B. H.; White, D. *J. Appl. Phys.* **1986**, *60*, 3772–3.
(33) Suits, B. H.; Lutz, J. L. *J. Appl. Phys.* **1989**, *65*, 3728–30.
(34) Miller, J. B. Unpublished results.
(35) Jackson, P.; Clayden, N. J.; Walton, N. J.; Carpenter, T. A.; Hall, L. D.; Jezzard, P.; Wiggins, C. *10th EENC*; Veldhoven, The Netherlands, May 28–June 1, 1990, Abstract C.6.
(36) Miller, R. S.; Paul, I. C.; Curtin, D. Y. *J. Am. Chem. soc.* **1974**, *96*, 6334–9.
(37) Lin, C.-T.; Paul, I. C.; Curtin, D. Y. *J. Am. Chem. Soc.* **1974**, *96*, 3699–701.
(38) Miller, R. S.; Curtin, D. Y.; Paul, I. C. *J. Am. Chem. Soc.* **1974**, *96*, 6340–9.
(39) Paul, I. C.; Curtin, D. Y. *Science* **1975**, *187*, 19–26.
(40) Duesler, E. N.; Kress, R. B.; Lin, C.-T.; Shiau, W.-I.; Paul, I. C.; Curtin, D. Y. *J. Am. Chem. Soc.* **1981**, *103*, 875–9.
(41) Lin, C.-T.; Curtin, D. Y.; Paul, I. C. *J. Am. Chem. Soc.* **1974**, *96*, 6199–200.
(42) Chiang, C. C.; Lin, C.-T.; Wang, A. H.-J.; Curtin, D. Y.; Paul, I. C. *J. Am. Chem. Soc.* **1977**, *99*, 6303–8.
(43) Miller, R. S.; Curtin, D. Y.; Paul, I. C. *J. Am. Chem. Soc.* **1974**, *96*, 6329–34.

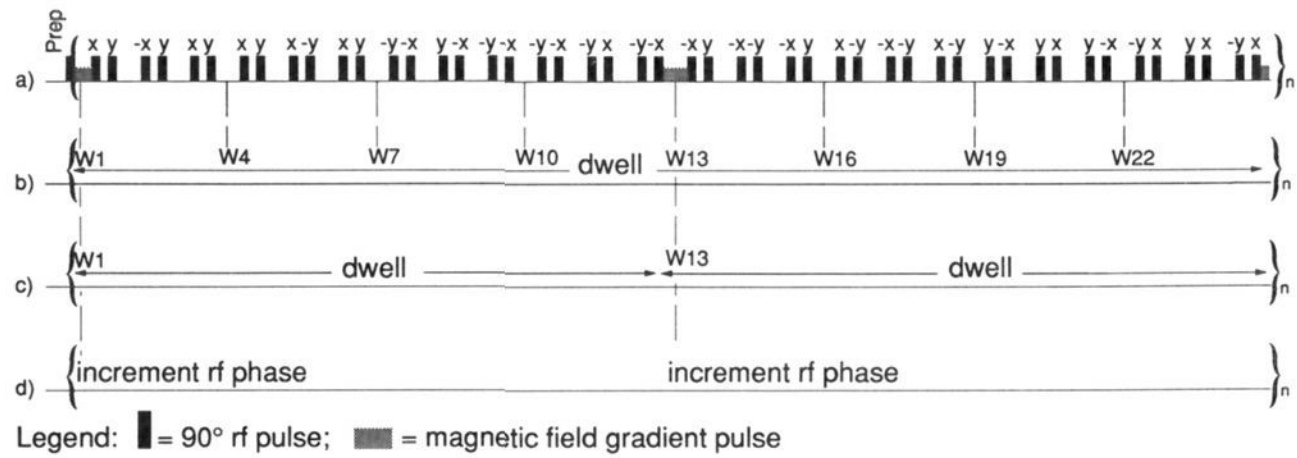

Figure 1. (a) The CMG-48 line-narrowing sequence. Depending upon the experimental needs, two different signal acquisition methods were used: (1) For an increased signal-to-noise ratio, all I_z windows, W1, W4, etc., are sampled (b) and the results added in the frequency domain. (2) For greater spectral width, only two I_z windows are sampled (c) and the dwell time is one-half of the cycle time. Finally, to offset the image from zero-frequency glitches, the base phase of all rf pulses is incremented by a constant amount, typically 30°, at the times indicated in trace d.

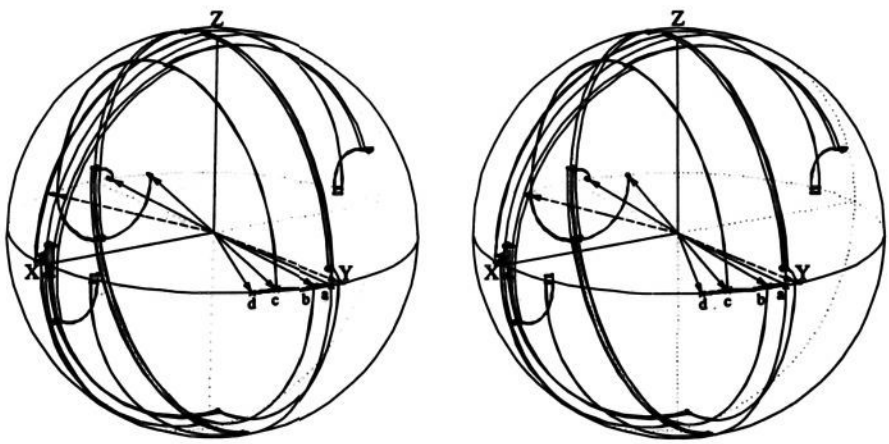

Figure 2. A stereodiagram showing the behavior of the ^1H spin magnetization in the rotating frame for a pair of dipolar coupled spins for a 90_x preparation pulse and one cycle of the CMG-48 sequence shown in Figure 1a. Thin portions of the line denote the evolution of the magnetization during an rf pulse whereas thick portions indicate evolution during a window. Some features of interest include the application of the gradient pulse in windows W1 and W13, Figure 1a, and the signal acquisition in the I_z windows, Figure 1b. The first portion of W1 starts at (a) on the y-axis and ends at (b). The gradient during W13 starts at (b) and ends at (c). The second portion of W1 starts at (c) and ends at (d). Vectors representing the nine acquisitions in the eight I_z windows (W1 is divided into two portions) are drawn from the origin to the calculated spin magnetization. The vectors are coded according to clockwise (—) or counterclockwise (– –) evolution about the z-axis.

in one dimension as ammonia gas is passed over the top of the bed. The rate of conversion into ammonium toluate is obtained and analyzed with a simultaneous diffusion with reaction model for a slab.

Experimental Methods

Instrumentation. A homemade 100-MHz (^1H) NMR spectrometer with an 11 cm bore solenoidal Oxford[54] magnet was used for all experiments. A subset of Chemagnetics[54] CMX console was used to control some aspects of the experiment: rf pulse timing and digital phase shifting, gradient pulse timing and amplitude, and signal digitization. For the 10-mm solenoidal rf coil used herein, the 90° pulse length was 3 μs. The short windows of the multiple pulse sequence are 2 μs and the long windows are 7 μs. The axis of the gradient coil is aligned with the static magnetic field. Driven by a Techron[54] Model 7560 audio amplifier, the 5-μs gradient pulses have an effective average gradient of 0.042 T m^{-1}, as determined from the image and the known sample geometry; a delay of 2 μs is allowed for gradient pulse decay before the next rf pulse is applied. Additional features of the gradient coil have been published elsewhere.[18,19] One-dimensional images of toluic acid were obtained with a stationary sample. For two-dimensional images, the 4-bromobenzoic acid crystal was rotated about an axis orthogonal to the gradient direction in constant increments of either 3° or 6° over a range of 180° to collect sets of 60 or 30 one-dimensional projections, respectively.

The multiple-pulse sequence used herein, CMG-48, is composed of 48 rf pulses, two pulsed magnetic field gradients, and eight potential observation windows per cycle, as shown in Figure 1.[3] This 48-pulse sequence was designed so as to reduce the resonance line broadening effects of dipolar coupling and chemical shifts such that the solid-state ^1H line shape is transformed into a single narrow resonance. The pulse sequence has also been designed such that magnetic field gradients can be applied in selected windows without adversely affecting the line-narrowing properties of the sequence.

There are two procedures commonly used to assess the performance of multiple-pulse sequences: average Hamiltonian theory and density matrix calculations.[11] The 48-pulse sequence has already been analyzed with average Hamiltonian theory;[3] important results are that dipolar coupling and chemical shifts effects are eliminated to second order, leaving only pulsed magnetic field interactions in the toggling frame. In the pulse sequence are windows in which no rf pulses are applied. In the toggling frame of reference, the Hamiltonian switches through a sequence of states; in particular, those windows for which the linear spin operator is I_z are denoted I_z windows and all of the longer I_z windows are labeled in Figure 1 as W1, W4, etc. Sampling the spin magnetization once per multiple phase cycle leads to a rather narrow effective spectral width. However, "oversampling", that is, sampling more than once during the cycle, reduces the dwell time and yields a larger spectral width which is particularly advantageous for imaging where we have control over the strength of the gradient Hamiltonian.[44]

We give here results of a density matrix calculation of the 48-pulse sequence for the purpose of demonstrating that dipolar coupling is indeed diminished and that the labeled windows in Figure 1 are appropriate for sampling spin magnetization, provided certain precautions are taken

(44) Cory, D. G.; Garroway, A. N.; Miller, J. B. *J. Magn. Reson.* **1990**, *87*, 202.

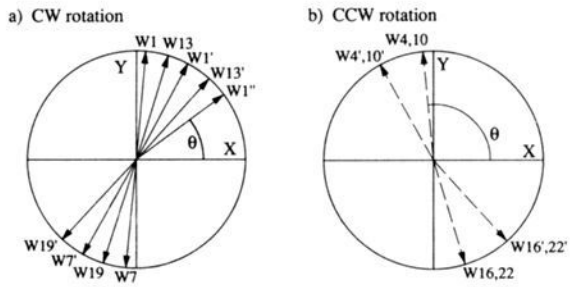

Figure 3. The calculated spin magnetization in the xy-plane of the rotating frame for the I_z windows for two cycles following a 90_x preparation pulse. The labels W1 and W4 indicate magnetization sampled in the first two I_z windows of the pulse sequence shown in Figure 1a. A prime denotes windows in the second cycle. In a, the spin magnetization is evolving, in the indicated windows, in a clockwise rotation about the z-axis, whereas evolution is counterclockwise for the other windows, shown in b.

during data processing. The results are displayed in the form of a stereodiagram[45] in Figure 2. The calculation is for a pair of protons separated by 2 Å; the internuclear vector connecting the two protons is at 90° relative to the applied magnetic field. (A two-spin system was chosen for simplicity of calculation and suffices herein for its pedagogic value. To fully assess the dipolar decoupling efficiency of the pulse sequence, a larger spin system is required.) Other parameters of the calculation are the following: Larmor frequency = 100 MHz, chemical shift = 0 Hz, 90° pulse length = 2 μs, τ = 5 μs, cycle length = 360 μs, preparation pulse = 90_x, gradient × position = +0.1 mT, gradient duration in W13 = 8 μs, interval between calculated magnetization vectors = 100 ns, and the radius of the sphere in Figure 2 is set equal to M_0.

The trace in Figure 2 shows the evolution of the spin magnetization in the rotating frame for one complete cycle of the line-narrowing pulse sequence starting from a magnetization vector oriented along the z-axis. With a 90_x preparation pulse and a slight increase in the resonance frequency due to the pulsed magnetic field gradient, the magnetization will, over the course of one multiple-pulse cycle, evolve from $+y$ toward $+x$; specifically, magnetization evolves from the point labeled (a) to (d), as shown in the figure. The evolution from (a) to (b) corresponds to that induced by the gradient applied immediately after the preparation pulse during W1. Similarly, the evolution between (b) and (c) and between (c) and (d) is due to the gradient in W13 and the second portion of W1, respectively. The fact that the spin magnetization is evolving through points (a) through (d) without diminishing in magnitude shows that the effect of dipolar coupling has been greatly eliminated. The spin system is evolving, if sampled in windows W1 and W13, to yield a single, narrow resonance at an offset frequency (relative to the carrier frequency) given by the gradient × position product. The effect of dipolar coupling is evident in the cusps at points (b) and (c). During the evolution from (a) to (b), the effect of dipolar coupling is to convert some magnetization into dipolar order, thus reducing the length of the magnetization vector. (In the absence of a gradient and a line-narrowing sequence, magnetization would evolve from $+y$ to $-y$ and would never have a component along $\pm x$. The Fourier transform would yield the familiar two-line pattern for a dipolar-coupled spin pair at a fixed orientation with respect to the magnetic field.) The cusps at (b) and (c) are a result of the line-narrowing sequence, a sequence which yields the desired result, magnetization vectors of length $|M_0|$ in W13 and at point (d) for this simple pedagogical case of a two-spin system.

Also shown in Figure 2 are nine vectors drawn from the center of the sphere to the calculated spin magnetization at the end of each labeled window shown in Figure 1, the windows that are termed I_z windows in the average Hamiltonian analysis. All nine vectors terminate near the surface of the sphere, hence, $|M|$ for each vector is nearly $|M_0|$. Also, all nine vectors lie in the xy-plane; thus, the magnetization can be detected by an rf solenoid perpendicular to the applied magnetic field. In summary, the results of the density matrix calculation for one special spin system (two dipolar coupled protons yield an inhomogeneous spin system) show that dipolar coupling is nearly eliminated and that magnetization can be sampled in selected windows from which one can obtain a narrow resonance.

When all I_z windows are sampled, as indicated in Figure 1b, there are two apparent rotations of the spin magnetization, clockwise and counterclockwise about the z-axis. This property is somewhat evident in Figure 2, but more obvious in a two-dimensional representation shown

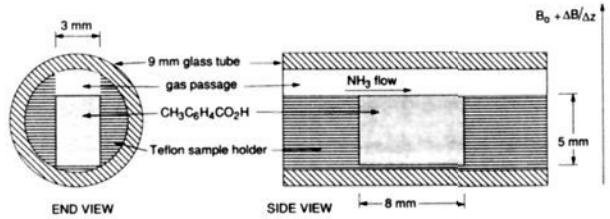

Figure 4. Sample holder for one-dimensional imaging of powdered toluic acid reacting with ammonia gas.

in Figure 3 in which only the spin magnetization vectors that are to be sampled are shown. Commonly used phase-cycling schemes, such as CYCLOPS,[46] for the preparation pulse and receiver that involve rerouting of "real" and "imaginary" signal components will average to zero the signal from either one or the other rotation, clockwise or counterclockwise, depending on the relative variation of transmitter and receiver phases, under the assumption of a constant receiver phase during the signal acquisition following each preparation pulse. Therefore, we accumulate data from 90_x and 90_{-x} preparation pulses separately from that due to 90_y and 90_{-y} preparation pulses. After acquisition, the two data sets are added together in the frequency domain according to the following procedure. First, the data from each I_z window are baseline corrected, Fourier transformed, and phase corrected to zeroth order only. The spectra from the counterrotating I_z windows are reflected about the carrier frequency. Then, all 16 spectra are summed in the frequency domain. The final result has a spectral width given by 1/dwell (see Figure 1b) and a theoretical gain of $\sqrt{8}$ in the signal-to-noise ratio relative to acquiring signal in just one I_z window. In practice, the strategy was useful for the two-dimensional imaging of the small 4-bromobenzoic acid crystal. However, there is a significant additional time and computer storage overhead encumbered for the postacquisition data processing associated with all 30 or 60 projections. Adding the data in the time domain rather than in the frequency domain would yield a modest overall time savings; however, we note that the phase corrections actually used are similar, but not identical, to those shown in Figure 3. By oversampling, we introduce residual Hamiltonians, i.e. chemical shift, that are not averaged to zero within a subcycle. This creates phase shifts not accounted for in the simulation for which the assigned chemical shift is zero.

Two slightly different forms of sampling the CMG-48 sequence were used depending upon the experimental requirements: (1) Increased spectral width by oversampling was used for the powdered toluic acid experiments. (2) Increased signal-to-noise by summing the quadrature signal from all I_z windows, as described above, was used for most 4-bromobenzoic acid crystal work. For all NMR experiments, the base phase of the rf pulses was incremented by a constant amount, typically 30°, applied synchronously with the gradient pulse, so as to shift the image away from zero frequency. (Small missettings of spectrometer parameters lead to image distortions or "glitches" near zero frequency.) The phase increment was applied during the I_z windows W1 and W13, as shown in Figure 1d.

The two-dimensional images were calculated with the filtered back-projection reconstruction algorithm.[47] For the one-dimensional imaging experiments of powdered toluic acid, a much larger sample was used and the signal-to-noise ratio was much more favorable. Then, the pulse sequence shown in Figure 1a was used with the acquisitions as indicated in Figure 1c.

Samples. A mixture of 9.85 mol % ammonia in argon from Scientific Gas Products was used for ammonia exposures, all of which were performed at room temperature and with an absolute pressure of about 1 atm. Note: The use of ammonia diluted in argon was a happenstance based upon convenient availability; however, it is likely that dilution reduced the rate of reaction so that monitoring the reaction by NMR imaging was made easier. 4-Bromobenzoic acid was purchased from Aldrich and recrystallized from acetone. A crystal with dimensions of [6.6 to 7] × 4 × 0.4 mm was selected and attached to a glass capillary tube with a minimum amount of poly(α-cyanoacrylate) (superglue). The crystal was placed in a low-velocity NH_3/Ar gas stream, about 0.002 L s^{-1}, in a laboratory hood. During one NH_3 exposure, a portion of the crystal broke off and was recovered, but not used. Mounted in the sample holder and near the crystal was a capillary tube containing a few crystals of ferrocene. The purpose of the ferrocene was to provide a readily observable marker in the 1D projections; this marker was used to align the projections prior to the back-projection reconstruction. For projec-

(45) Butler, L. G. *J. Magn. Reson.* **1991**, *91*, 369–9.

(46) Stejskal, E. O.; Schaeffer, J. *J. Magn. Reson.* **1974**, *14*, 160–9.
(47) Brooks, R. A.; Di Chiro, G. *Radiology* **1975**, *117*, 561–72.

tions of the unreacted crystal in which the 1D image of the marker was separate from that of the crystal, the peak height of the marker was slightly smaller than that of the crystal. The ferrocene marker was also used to normalize the intensity images taken before and after ammonia exposure.

Toluic acid (Aldrich) was used as received in the form of a fine powder. A 78-mg sample of toluic acid was packed into the sample holder, shown in Figure 4. Tygon tubing was used to connect the sample holder, while in the NMR probe in the magnet, to the NH_3/Ar supply. A flow rate of 0.002 L s^{-1} was used. Evidence that the packing of powdered toluic acid is uniform and that all of the toluic acid powder is exposed to ammonia gas is provided by the results of saturation–recovery NMR images taken before and after ammonia exposure and shown in Figure 5, spectra a and c, respectively. The relaxation delays for both experiments are 0.05, 0.1, 0.3, 0.5, 1, 3, 5, 10, 30, and 50 s. Small deviations from a rectangular profile are most likely due to either packing and/or sample holder imperfections. After exposure to ammonia gas, the sample holder was reweighed. A mass gain of 9 mg indicated that the reaction to form ammonium toluate proceeded to at least 92% conversion, perhaps more as some traces of ammonium toluate were found in the tubing downstream from the sample holder. The increase in the equilibrium magnetization, calculated from spectra a and c in Figure 5, also indicates at least 90% conversion of the sample to ammonium toluate. NMR images for the first few minutes of the reaction are shown in Figure 5b; clearly the top layers are reacting faster than the bottom layers.

Gas–Solid Reaction Modeling. Two schemes were considered for modeling the one-dimensional NMR imaging data for reaction of ammonia with powdered toluic acid. Finite element analysis has the advantage in that the spatial information contained within the NMR images is retained at the cost of computation complexity. Alternatively, the spatial information can be disregarded by summing over all frequency elements (equivalently, over all layers) at each point in time. The summed data, with normalization, yield the extent of conversion to ammonium toluate as a function of time. The problem of modeling the extent of conversion as a function of time is well-known in the chemical engineering literature and analysis schemes have been developed.

Because of the ease of implementation, the reaction of ammonia and powdered toluic acid is analyzed by using a simultaneous diffusion with reaction model and with the assumption that the reaction is first order in both reactants. In this model, the total conversion of toluic acid to ammonium toluate is modeled with two adjustable parameters, the apparent reaction rate constant and the effective diffusivity of ammonia gas through the powdered toluic acid. In principle this is a rather complicated boundary value problem involving two coupled nonlinear partial differential equations. With the assumption of a pseudo steady state for the gas reactant concentration and appropriate integral transformations, the problem can be reduced to a much simpler initial value problem of coupled ordinary differential equations.[48] Then, a pair of equations can be derived that, based on the cumulative ammonia gas concentration in the sample, give the extent of the reaction at a particular rate. To calculate the extent of reaction as a function of time requires solving an initial value problem for cumulative ammonia gas concentrations ranging from near zero to the gas-phase ammonia concentration. Note that it is not necessary to measure the ammonia gas concentration in the sample. Instead, the connection between experiment and the simultaneous diffusion with reaction model rests with the extent of conversion of toluic acid to ammonium toluate as a function of time. Also, the equations listed below are from Dudukovič for the particular case of a slab exposed to gas on one side and are written, for the most part, in dimensionless quantities.

For a given cumulative ammonia gas concentration, the extent of conversion, X, and the corresponding reaction time, t in seconds, are given by

$$X = W(\phi)/\phi \tag{1}$$

$$t = \frac{\phi}{kC_A^0 Bi_m}\left[W(\phi) + \frac{Bi_m}{\phi}Y(\phi)\right] \tag{2}$$

where ϕ is a dimensionless modulus for a gas–solid reaction

$$\phi = (kC_S^0/D_e)^{1/2}L \tag{3}$$

and where C_S^0 is the initial toluic acid concentration in mol cm^{-3}, k is the apparent reaction rate constant in mol^{-1} cm^3 s^{-1}, D_e is the effective diffusivity in cm^2 s^{-1}, and L is the depth of the toluic acid sample in cm. Other constants in eq 2 are C_A^0, the initial concentration of ammonia in the bulk gas phase in mol cm^{-3}, and Bi_m, the Biot number for mass transfer. The Biot number (dimensionless) is defined as (k_mL/D) where k_m is the mass transfer coefficient to a solid; the Biot number is evaluated using standard equations for mass transfer to slabs.[49]

The remaining quantities in eqs 1 and 2, ξ', W, Y, are elements of an initial value problem that is given by the following equations for a slab geometry

$$\partial Y/\partial \xi' = W \tag{4}$$

$$\partial W/\partial \xi' = 1 - e^{-Y} \tag{5}$$

where Y is a dimensionless quantity representing the cumulative ammonia concentration in the sample, W is a dimensionless independent variable, and ξ' is a dimensionless distance that ranges from zero to ϕ. The initial conditions are $\xi' = 0$, $W = 0$, and $Y = Y_0^i$ $(i = 1, 2, 3, ...)$, where the Y_0^i are a set of guessed values for dimensionless cumulative ammonia concentration in the toluic acid bed at $\xi' = 0$. Typically, the set of guessed dimensionless cumulative ammonia concentrations consists of 30 elements ranging from 0.01 to 20; this suffices to cover times ranging from near zero to about 8000 s for the rate constant and apparent diffusivity found herein. For each Y_0^i, eqs 4 and 5 are numerically evaluated with 4th and 5th order Runge–Kutta methods.[50] For each Y_0^i, a conversion factor, X, and a corresponding time, t, are obtained from eqs 1 and 2, respectively, for $\xi' = \phi$. From the 30 calculated pairs of X and t, a smooth curve is interpolated using a spline fit. The two unknowns, k and D_e, are then determined by fitting the experimental rate of conversion to the smooth curve where the optimization is done using the Levenburg–Marquardt nonlinear least-squares algorithm.[51,52]

One way to illustrate the simultaneous diffusion with reaction model for the ammonia and toluic acid reaction is to plot the time to 50% conversion as a function k and D_e, as shown in Figure 6. Actually, two separate contour plots are given in Figure 6; one plot is for a 5-mm slab of toluic acid as used herein, while a second overlaying plot is for a hypothetical 50-mm slab. Parameters used to generate both contour plots are as follows: $C_A^0 = 4 \times 10^{-6}$ mol cm^{-3}, $C_S^0 = 0.00437$ mol cm^{-3}, and $Bi_m = 83$. Three different regimes are evident from this plot. In one regime, the effective diffusivity is so slow that the time to 50% conversion, for a given slab thickness, is determined only by diffusion. In another regime, the reaction rate constant is so slow that k becomes the limiting parameter. Finally, there is an intermediate regime where slight changes in either k or D_e can affect the time to 50% conversion. It is in this intermediate regime where the fitting procedure described above to determine k and D_e is effective. For example, in the diffusion limited regime for $L = 5$ mm and $D_e = 10^{-6}$ m^2 s^{-1}, reactions with a rate constant of 10^{-3} mol^{-3} m^3 s^{-1} or greater all have the same 50% conversion time of about 4000 s and plots of conversion versus time are very similar. Thus in the diffusion limited regime, it is not possible to determine the reaction rate constant using the procedure described above. A finite element analysis, using information from the top few layers to determine k and from the bottom layers to determine D_e, would then be preferred. The conditions for the toluic acid reaction studied herein are such that the analysis given above is adequate to allow us to extract both a reaction rate constant and an effective diffusivity.

Results

Herein, the results for two separate sets of experiments are described. First, a crystal of 4-bromobenzoic acid is imaged in two dimensions by the use of a recently developed NMR line-narrowing sequence. The crystal is then exposed to ammonia gas and the progress of the reaction is monitored. Unfortunately, the NMR imaging results show that the crystal is of poor quality as reactions are observed across the face of the crystal. Nevertheless, the experiment is successful in that NMR imaging is used to follow the anisotropy of chemical reaction and to quantify the extent of conversion. In the second experiment, a bed of powdered toluic acid is imaged in one dimension as ammonia gas is passed over the top of the bed. The rate of conversion into ammonium toluate is obtained and analyzed with a simultaneous diffusion with reaction model for a slab.

(48) Dudukovič, M. P. *AIChE J.* **1976**, *22*, 945–7.

(49) Froment, G. R.; Bischoff, K. B. *Chemical Reactor Analysis and Design*; Wiley: New York, 1979.

(50) Hildebrand, F. B. *Introduction to Numerical Analysis*, 2nd ed.; Dover: New York, 1987.

(51) Bevington, P. R. *Data Reduction and Error Analysis for the Physical Sciences*; McGraw-Hill: New York, 1969.

(52) Press, W. H.; Flannery, B. P.; Teukolsky, S. A.; Vetterling, W. T. *Numerical Recipes*; Cambridge University Press: Cambridge, 1986.

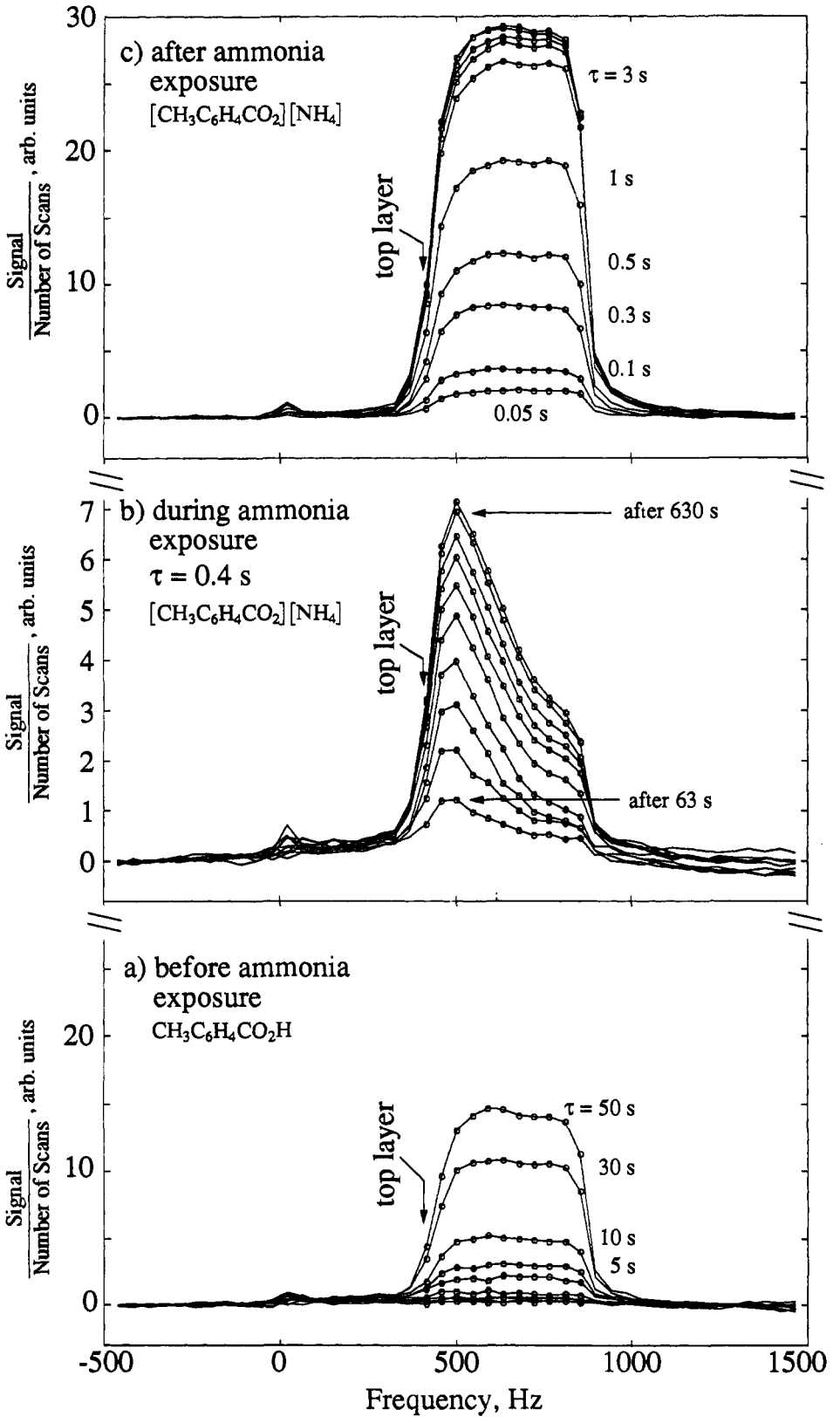

Figure 5. Combination 1D ^1H NMR imaging and saturation–recovery spectra for powdered toluic acid in the sample holder shown in Figure 4: before ammonia exposure (a), during the first few minutes of ammonia exposure (b), and after ammonia exposure (c). The relaxation delays for the saturation–recovery spectra are shown next to the corresponding spectrum, space permitting; for Figure 5b, the relaxation delay is 0.4 s. A small zero-frequency glitch is evident in all figures. The line width for the unreacted toluic acid in the absence of a pulsed field gradient is less than or equal to the digital resolution used here of 43 Hz. There is appreciable signal intensity at eleven different, discrete frequencies that are separated by the digital resolution of the experiment. These eleven frequencies are then assigned as eleven resolvable layers in the sample and are denoted here by (O), and the frequency corresponding to the top layer is so labeled. The lesser intensity of the extreme bottom and top layers is due to partial filling of those layers, i.e., an uneven top layer of powdered toluic acid in the sample holder.

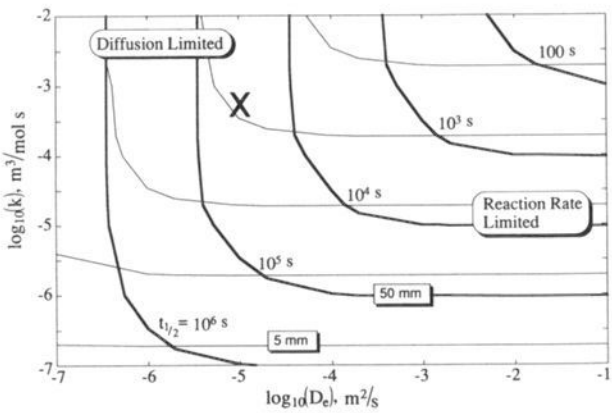

Figure 6. Two contour plots showing the effect of diffusivity and reaction rate upon the time required to achieve 50% conversion. Time to 50% conversion, $t_{1/2}$, for samples with two different thicknesses are shown: 5 mm (thin lines) and 50 mm (thick lines). The large "X" represents $k = 5 \times 10^{-4}$ mol^{-1} m^3 s^{-1} and $D_e = 1.0 \times 10^{-5}$ m^2 s^{-1}. For a 5-mm slab with these values for k and D_e, the reaction is not fully limited by either parameter, since an increase in either will reduce the time for conversion. However, for a 50-mm slab, the reaction is fully diffusion limited in that an increase in k would have no effect on the 50% conversion time.

4-Bromobenzoic Acid Crystal. A photograph of the 4-bromobenzoic acid crystal before exposure to ammonia is shown in Figure 7a. On the basis of earlier morphological studies,[39] the crystal face shown in the plane of the picture is believed to be (100), the face that reacts least rapidly with ammonia.

An inversion-recovery experiment showed that the ^{1}H T_1 of unreacted 4-bromobenzoic acid crystals is quite long, 140 s. A separate sample of powdered 4-bromobenzoic acid was exposed to ammonia; the ^{1}H T_1 of ammonium 4-bromobenzoate is 3 s. Thus, T_1 is an appropriate contrast agent for reacted and unreacted 4-bromobenzoic acid. However, the long T_1 of the unreacted form makes it quite difficult, though not impossible, to image a crystal of 4-bromobenzoic acid.

Shown in Figure 8 is the 2D ^{1}H NMR image of the unreacted 4-bromobenzoic acid crystal and the ferrocene marker. The irregular shape of the ferrocene marker may be a result of the very few ferrocene crystals in the capillary tube. The ^{1}H T_1 of the ferrocene marker is 8 s. The general features of the crystal NMR image agree well with the photograph. The NMR image is mostly rectangular with a slight trapezoidal distortion. Most of the crystal has an uncorrected intensity value between 20 and 40% relative to the ferrocene marker, as shown in Figure 8a. When corrected for T_1 saturation effects for the ammonium 4-bromobenzoate signal, the intensity levels range between 27 and 55% to the ferrocene marker. Thus, by NMR studies, the crystal is relatively flat, an observation that can be seen more easily in the grey scale image shown in Figure 8b. Finally, the superglue used to mount the crystal does not contribute excessively to the NMR image.

The crystal was exposed to ammonia for 12 h. During this exposure, a portion of the crystal broke off from the main body. The photograph, not shown here, showed some whitening or powdering at two corners corresponding to the upper left and upper right of the crystal as shown in Figure 7b. Two NMR images were acquired using relaxation delays of 5 and 30 s, respectively. In neither image was the entire body of the crystal observed. Rather, there was a weak signal in the center and at one spot displaced to the left of center. The edges of the crystal, the region of the expected reaction, were not observed in the NMR images.

The crystal was then exposed to ammonia for an additional 24 h. The photograph, shown in Figure 7b, shows whitening or powdering across most of the face of the crystal. This is not the same behavior seen (visually) in previous reactions of 4-bromobenzoic acid crystal[39] where the edges of the plate-like crystal show significant reaction, in the form of white, opaque regions, before reaction is evident upon the face. This observation suggests that the crystal used here is of poor quality or, less likely, has a different morphology. Nevertheless, the NMR image, shown in Figure 9, is consistent with the optical observations. There is a weak signal across the entire face of the crystal with an uncorrected intensity ranging from 30 to 50% of the ferrocene marker. When corrected for saturation effects for both the ferrocene marker and ammonium 4-bromobenzoate, the corrected intensities range from 17 to 28% of the ferrocene marker. As for the images taken at 12 h, extra intensity is observed in the center and at a spot to the left of center. Also, a new region to the right of center, not observed at 12 h of ammonia exposure, has gained intensity. An image taken with a relaxation delay of 10 s also showed similar regions of reactivity to that found for a relaxation delay of 5 s; intensity is observed in various regions across the face of the crystal.

The two NMR images, Figures 8a and 9a, are plotted to the same scale based upon the peak intensity for the ferrocene marker. For data shown in Figure 9, no correction is made of the crystal signal intensity to account for the partial saturation of the ferrocene marker ($T_1 = 8$ s); applying a correction would reduce the overall "brightness" of the reacted crystal. Also, an exponential line broadening is applied to the 1D projections used to generate Figure 9, a and b. The gray scale palettes used in both Figures 8b and 9b have been arbitrarily and individually chosen to enhance details of each image.

We can estimate the extent of conversion of portions of the crystal from 4-bromobenzoic acid to ammonium 4-bromobenzoate

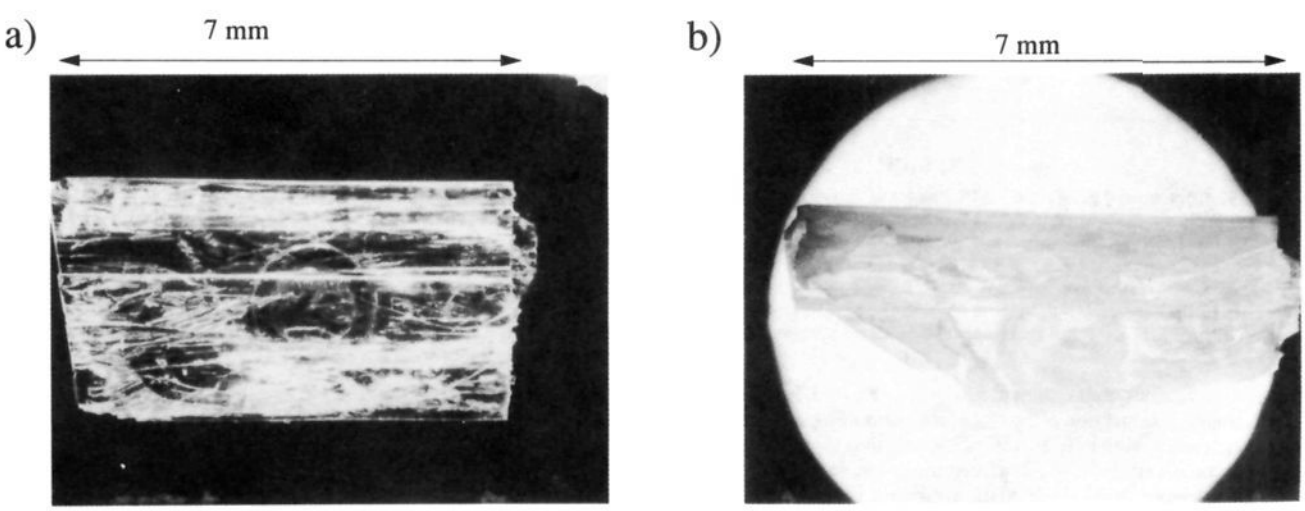

Figure 7. Photographs of a crystal of 4-bromobenzoic acid before (a) and after (b) exposure to ammonia gas. A portion of the crystal broke off during exposure, hence the reduced size in b. Not shown in either photograph is the ferrocene marker; in the NMR experiments, it lies below the crystal as shown in this orientation. Partially visible in the center of both photographs is the end of the glass capillary tube onto which the crystal is mounted.

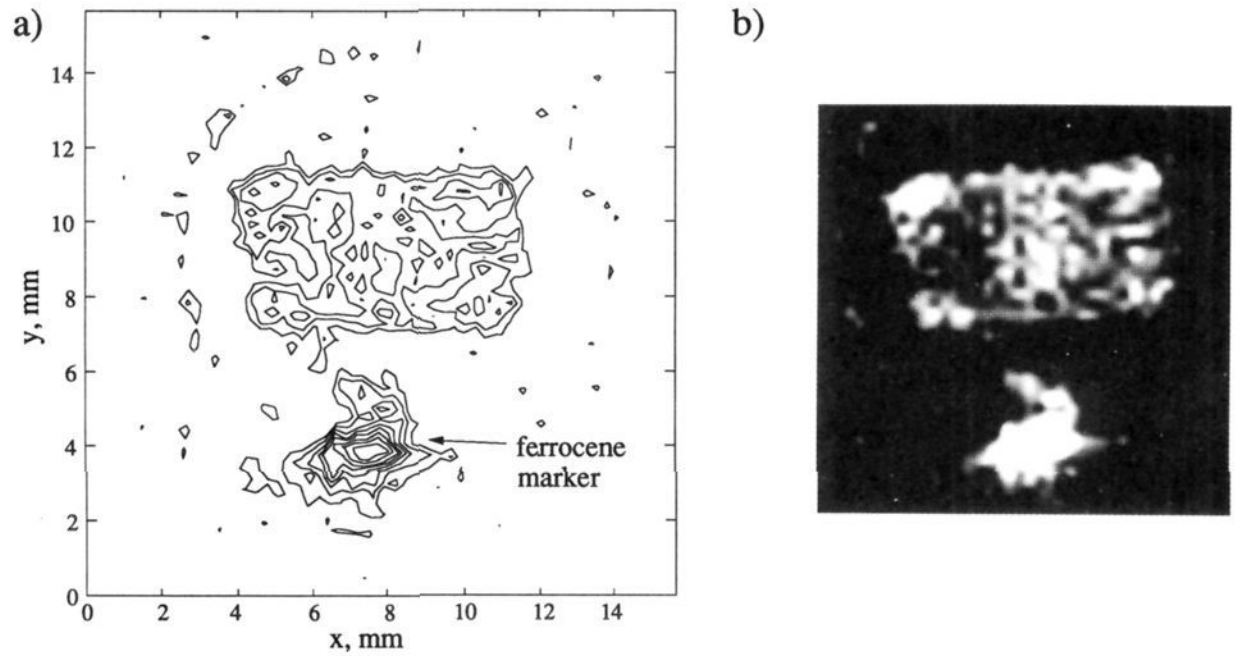

Figure 8. Contour and gray scale NMR images of a crystal of 4-bromobenzoic acid before exposure to ammonia gas. The image is reconstructed from 30 projections acquired in 60 h. Each projection consists of 40 acquisitions, sampled as shown in Figures 1b and 3, and obtained with a relaxation delay of 180 s. The data sets were processed as described earlier and without application of any line broadening. The contour levels are based on the most intense pixel of the ferrocene marker having an assigned intensity of 100%; contour levels are drawn at 20–90% levels in increments of 10%. The gray scale image intensity levels are arbitrary.

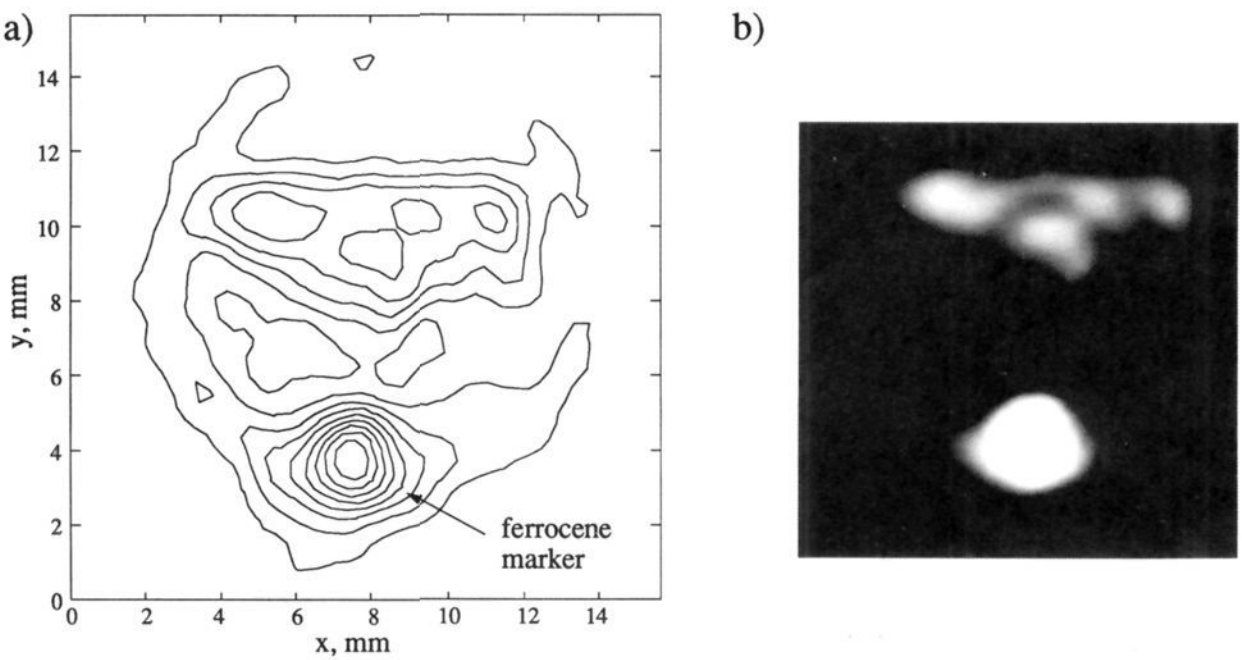

Figure 9. Contour and gray scale NMR images of a crystal of 4-bromobenzoic acid after exposure to ammonia gas for 36 h. The image is reconstructed from 60 projections acquired in 5.3 h. Each projection consists of 64 acquisitions, sampled as shown in Figures 1b and 3, and obtained with a relaxation delay of 5 s; however, only the data from windows labeled W1 and W13 were retained. The data sets were processed as described earlier and with an exponential line broadening of 33 Hz. The contour levels are based on the most intense pixel of the ferrocene marker having an assigned intensity of 100%; contour levels are drawn at 20–90% levels in increments of 10%. The gray scale image intensity levels are arbitrary. By referencing signal intensity to the ferrocene marker and making the necessary corrections for T_1 saturation effects and the increased number of protons in the product, we can estimate the extent of reaction. The more reactive regions of the crystal are about 40% converted from 4-bromobenzoic acid to the ammonium salt.

using the contour plots shown in Figures 8a and 9a and with corrections for saturation effects. Before ammonia exposure, most areas of the crystal had an intensity, relative to the ferrocene marker, of about 30% (41% after correction for saturation of 4-bromobenzoic acid) while after ammonia exposure the more reacted portions of the crystal have an intensity of 50% (28% after correction for saturation of ferrocene and ammonium 4-bromobenzoate), where we assume that all of the signal from the reacted crystal is due to ammonium 4-bromobenzoate. The extent of conversion is then given by

$$\frac{M^{eq}([BrC_6H_4CO_2][NH_4]) = 28\%}{M^{eq}(BrC_6H_4CO_2H) = 41\%} \times \frac{5}{8} \times 100 = 43\% \text{ conversion} \quad (6)$$

where the factor of $^5/_8$ accounts for the change in the number

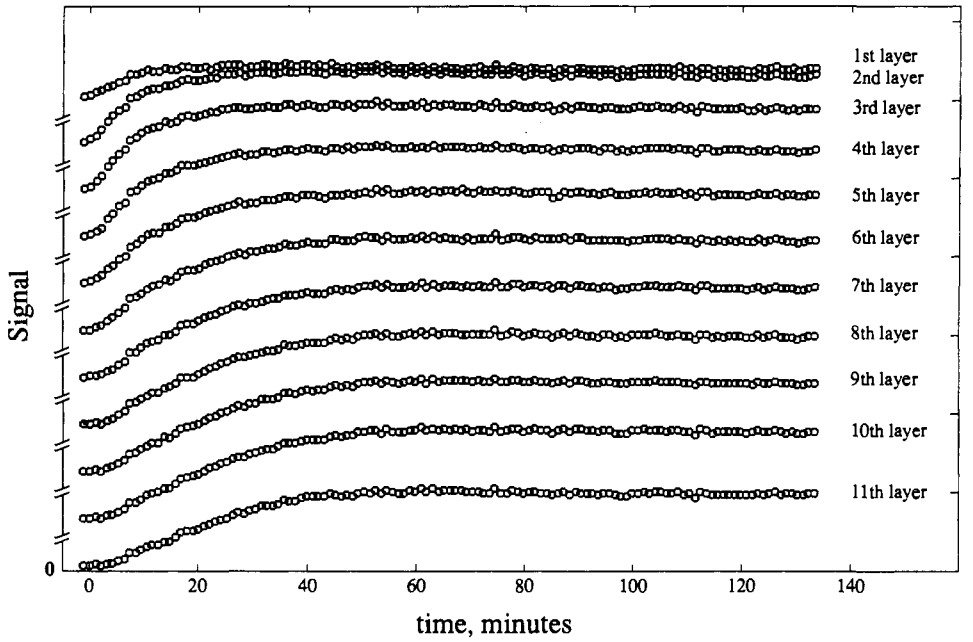

Figure 10. The results of 1D ^{1}H NMR images as a function of ammonia exposure for a packed bed of powdered toluic acid. The zero of the time axis corresponds to the beginning of ammonia exposure and the increment of the time axis is given by the time required to acquire and store each image. Each layer corresponds to a single-frequency region (see Figure 5) and has an initial signal intensity of about zero. The results for each layer are offset from each other for visual clarity.

of protons in the sample.

Powdered Toluic Acid. In this experiment, one-dimensional images are taken showing the reaction of a bed of toluic acid exposed to ammonia. The rate of conversion of toluic acid to ammonium toluate is controlled by factors such as the concentration of ammonia in the gas stream, the rate of reaction of ammonia with solid toluic acid, and the effective diffusivity of ammonia through the powdered sample. The goal of this experiment is to determine if parameters such as the rate of a reaction and the effective diffusivity of a component can be determined since these are factors that are important in a wide variety of reactions at interfaces. The difference in the ^{1}H T_1 between toluic acid and ammonium toluate (see Figure 5) was used to provide the contrast between the reactant and product of the gas–solid reaction. Thus, the relaxation delay was set to 0.4 s and only ammonium toluate contributes significantly to the NMR signal. With the line narrowing sequence shown in Figure 1c, but without the application of a magnetic field gradient, the full width at half height of toluic acid is less than the digital resolution of 43 Hz. When the pulse sequence and a pulsed magnetic field gradient are applied to a sample of toluic acid held in the sample holder shown in Figure 4, the image shown in Figure 5a is formed. The digital resolution of the 1D ^{1}H NMR images shown in Figure 5 is 43 Hz. Eleven data points define the images of the 5-mm toluic acid sample, corresponding to a spatial resolution of about 500 μm. Since the line width in the absence of a magnetic field gradient is less than the digital resolution, each data point in frequency space is labeled as a distinct layer in the toluic acid sample. Because of the relatively good sensitivity for imaging ammonium toluate, a 1D ^{1}H NMR image could be acquired and stored in slightly over 1 min (63 s). The first few minutes of the reaction are shown in Figure 5b.

The results from a series of 1D ^{1}H NMR images obtained as powdered toluic acid is exposed to ammonia gas are shown in Figure 10. Here, the relative signal strength at each frequency (corresponding to a separate layer) is plotted as a function of time. It is clear that all layers show an increase in signal strength corresponding to the production of ammonium toluate. On the basis of the mass gain and the NMR data, the conversion to ammonium toluate is essentially complete after 60 min of ammonia exposure.

The most interesting aspect of the data shown in Figure 10 is the effect sample depth has upon the rate of conversion. The upper layers, say layers 1–3, show signs of reaction nearly coincident with the beginning of ammonia exposure. In contrast, the bottom layer shows a noticeable delay before any reaction is detectable. Also the rate of conversion is slower for the bottom layers relative to the upper layers. On the basis of this observation, the rate of conversion depends not only upon the intrinsic rate of reaction of powdered toluic acid with ammonia but also upon the rate of diffusion of ammonia gas through the packed bed.

The total conversion of toluic acid to ammonium toluate as a function of time is given by summing over all layers shown in Figure 10 and is shown in Figure 11. Also shown in Figure 11 is the best fit of the conversion data to the simultaneous diffusion with reaction model. The adjustable parameters of the fit are the apparent reaction rate constant, k, and the effective diffusivity, D_e. The results are $k = 5\ (2) \times 10^{-4}$ mol^{-1} m^3 s^{-1} and $D_e = 1.0\ (4) \times 10^{-5}$ m^2 s^{-1}. The good fit to the data suggest the absence of significant temperature gradients in the bed. There is a small systematic deviation from the fit after about 4000 s. The decline is larger than can be attributed to sample having been blown out of the holder by the gas flow; at most, 1 mg was lost through this mechanism. Alternatively, a small temperature change together with a temperature-dependent ^{1}H T_1 may account for the systematic deviation.

Discussion

Neither the optical nor the NMR images for the reaction of a 4-bromobenzoic acid crystal with ammonia gas showed the expected reaction anisotropy. The most obvious explanation for the optical results is that the crystal quality is poor and that the reaction was occurring at numerous sites across the face of the crystal. Alternatively, this crystal of 4-bromobenzoic acid may have had a different morphology that that used by Paul and Curtin.[39] Nevertheless, the important result remains that the NMR images, which showed mostly uniform signal intensity, are consistent with the optical images which showed some signs of reaction across the face of the crystal. It has proved possible to image quite small samples with multiple pulse line narrowing by utilizing magnetization in all I_z windows. Thus, with a better quality single crystal showing, optically, a clear reaction anisotropy, one might reasonably expect to acquire NMR images that definitively reflect the anisotropy of the reaction occurring as described by Paul and Curtin.[39] The importance and utility of a

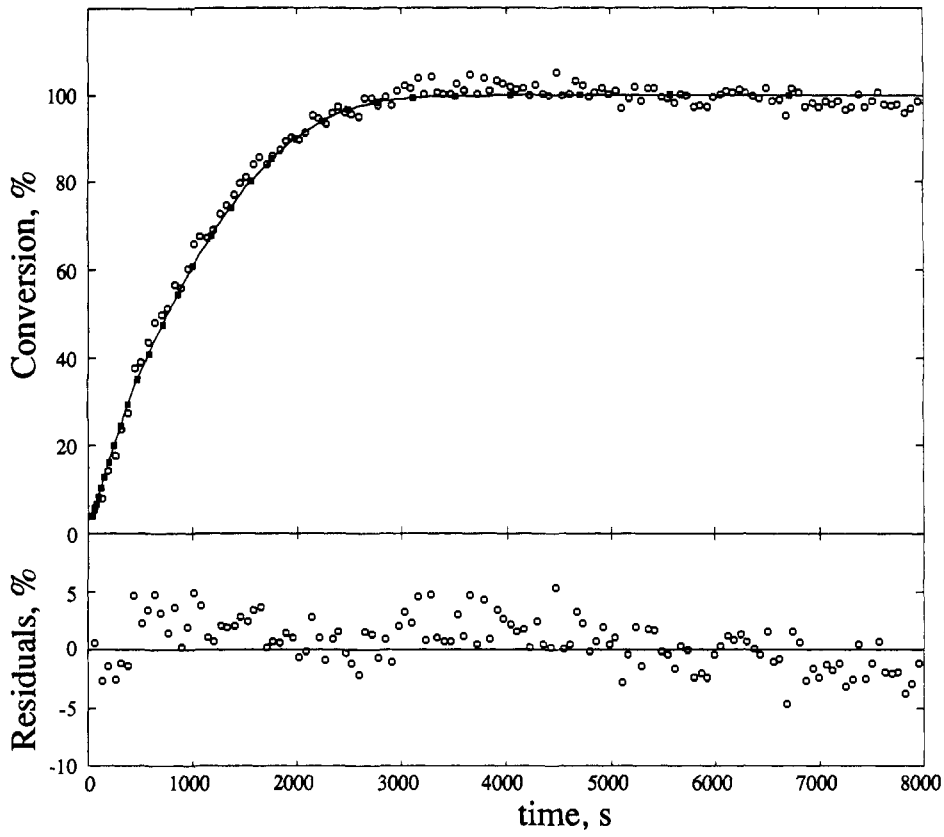

Figure 11. The total conversion of toluic acid into ammonium toluate is shown here as a function of ammonia exposure time. The data points (○) are taken from Figure 10 by summing over all layers and normalizing to 100% final conversion. The smooth curve through the data represents a spline fit to the calculated conversions, X, and reaction times, t, from eqs 1 and 2; the calculated points are shown (■). Important parameters in eqs 1 and 2 are as follows: $C_A^0 = 4 \times 10^{-6}$ mol cm^{-3}, $C_S^0 = 0.00437$ mol cm^{-3}, $Bi_m = 83$, and $L = 0.5$ cm. The residuals are shown below the main graph.

marker is stressed here, both to orient 1D projections and to scale images taken at different points along a reaction coordinate so that the extent of reaction can be obtained.

The reaction of a bed of powdered toluic acid with ammonia gas clearly shows reaction heterogeneity in the 1D ^{1}H NMR images. As expected, the top layers of the sample react more rapidly than do the bottom layers. A simple isothermal simultaneous diffusion with reaction model is sufficient to extract an apparent reaction rate constant and an effective diffusivity from the total conversion data; the porosity to tortuosity[53] ratio calculated from D_e is 0.54, which is reasonable for a loosely packed bed. The rate of conversion for this 5-mm sample is limited by both the rate of diffusion and the rate of reaction. In Figure 6, we show a contour graph for a 5-mm sample (thin lines) showing the time required to convert one-half of the sample as a function of both the apparent reaction rate constant and the effective diffusivity. (Also indicated in this plot is the point corresponding to the k and D_e values obtained herein.) An increase in either k or D_e would result in a faster conversion time. However, if the sample thickness is increased to 50 mm (thick contour lines), then an increase in k would not yield a faster conversion time; for this case, the conversion would be completely diffusion limited.

The reader will note that the spatial information contained in Figure 10 was, in fact, not used for the fit shown in Figure 11. A more sophisticated partial differential equation model, with split boundary conditions on the fluid-phase mass balance and perhaps requiring solution by finite element techniques, is necessary to fit the data shown in Figure 10. An analysis in that detail is beyond the scope of this present work, but is exactly what is needed to address more complex situations. For example, one can imagine samples with a temperature gradient for which one layer would have a different k and D_e than another layer.

Conclusions

Shown herein are the first 2D ^{1}H multiple-pulse NMR images following a chemical reaction for which the image contrast is T_1 rather than T_2. A multiple-pulse line-narrowing sequence is critical to image acquisition where broad lines are expected. Within the CMG-48 sequence, there are multiple windows which can be sampled so as to increase the signal-to-noise ratio of the image, thus enabling relatively small samples, such as crystals, to be imaged. The gas–solid reaction between ammonia and a crystal of 4-bromobenzoic acid was monitored optically and by NMR imaging. The expected reaction anisotropy was not seen, either optically or with ^{1}H NMR imaging, most likely due to poor crystal quality or an unexpected crystal morphology. Nevertheless, some anisotropy in the reaction was observed and the extent of reaction was obtained from the NMR images. The more reactive regions of the crystal are about 40% converted from 4-bromobenzoic acid to the ammonium salt. A gas–solid reaction between ammonia and a bed of powdered toluic acid showed clear reaction anisotropy; the top layers of the bed reacted faster than the bottom. The averaged conversion of toluic acid to ammonium toluate was analyzed with an isothermal simultaneous diffusion reaction model which yielded realistic D_e and k values.

It is clear that ^{1}H multiple-pulse NMR imaging yields images that detail chemical reactivity at interfaces. However, it is difficult to predict the full impact of NMR imaging of solid-state chemical reactions. On one hand, one-dimensional NMR images contain sufficient information to allow one to extract kinetic information. On the other hand, three-dimensional NMR images would have enabled monitoring the toluic acid/ammonia reaction at the boundaries of the sample holder. In either case, NMR imaging provides chemically useful information. Since the chemistry of interfaces is so important (for example, the curing of coatings, catalyst bed deactivation, adhesion, just to name a few), a tech-

(53) The ratio of average pore contour length to the length of the projection of the pore length vector along the principal axis of diffusion.
(54) Commercial products are mentioned for identification only.

nique which has the capability to selectively and quantitatively image a component within the interface will become extremely useful.

Acknowledgment. This work was supported in part by the Office of Naval Research. The sabbatical hospitality of the Naval Research Laboratory is gratefully acknowledged by one of us (L.G.B.). David G. Cory acknowledges a National Research Council/Naval Research Laboratory postdoctoral associateship.

Registry No. 4-Bromobenzoic acid, 586-76-5; ammonia, 7664-41-7; toluic acid, 25567-10-6.

Spectroscopic Evidence for the Formation of a Bridged Lithium Dicyclopentadienyl Lithiate Complex

M. Eiermann and K. Hafner*

Contribution from the Institut für Organische Chemie, Technische Hochschule Darmstadt, Petersenstrasse 22, D-6100 Darmstadt, Federal Republic of Germany. *Received May 22, 1991*

Abstract: One- and two-dimensional NMR and DNMR studies including ^{6}Li NMR prove the formation of a ferrocene-bridged lithium bis(vinylcyclopentadienyl)lithiate complex **8** in THF solution. Two different dynamic processes could be detected: the exchange of the ate-bound lithium ion with the solvent-separated lithium species and the intramolecular rotation of the hydrocarbon decks, involving the cleavage of the ate complex in the transition state. From the activation parameters of both processes derived from NMR line shape simulation it is shown that the lithium ion exchange process should proceed without the loss of the chelate conformation.

Exceptional interest in the structures of organolithium compounds has been focused on their structures in solution, since they have importance as key intermediates in organic synthesis. The interaction between the lithium ion and the carbanion has been investigated with a variety of spectroscopic methods.[1] From the NMR techniques, ^{6}Li,^{1}H heteronuclear Overhauser effect spectroscopy was shown to be a useful tool to detect short lithium–hydrogen distances.[2]

Prompted by a recent study[3] on the formation of ate-type lithium cyclopentadienide complexes, e.g., **1**, and its structure in THF solution, we herein wish to report our results concerning a ferrocene-bridged analogue. Within conductivity measurements of alkalimetal cyclopentadienides the existence of a $Li(C_5H_5)_2^-$ species as a triple ion has been already discussed earlier.[4]

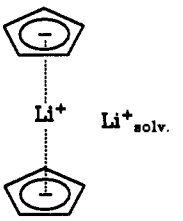

1

In the course of our studies on kinetically stabilized vinylogous 6-cyclopentadienylpentafulvenes[5] as potential precursors for the synthesis of dinuclear transition-metal complexes, 6-cyclopentadienyl-6-methylpentafulvene **4** was prepared from sodium *tert*-butylcyclopentadienide (**2**) and *N*,*N*-dimethylmethoxyacetiminium methanosulfate (**3**) as a mixture of four structural isomers with *tert*-butyl substituents in β-position with respect to the bridge. Whereas treatment of **4** with 2 equiv of lithium 2,2,6,6-tetramethylpiperidide (LiTMP) furnishes dilithium ethylene-1,1-bis(3-*tert*-butylcyclopentadienide) (**5**), the reaction with potassium *tert*-butanolate yields potassium 3-*tert*-butyl-1-(2-*tert*-butyl-6-methyl-6-pentafulvenyl)cyclopentadienide (**6**) exclusively. Both compounds were characterized by ^{1}H and ^{13}C NMR spectroscopy, establishing symmetrical structures and detecting rapid rotation of the five-membered rings vs the bridge carbon atom at room temperature in the NMR time scale.

Addition of anhydrous ferrous chloride to a solution of **6** in THF leads to the formation of a mixture of various isomeric ferrocenes **7**. Simple column chromatography on basic alumina allows the isolation of one isomer, 3,3′-di-*tert*-butyl-1,1′-bis-(*Z*-2-*tert*-butyl-6-methyl-6-pentafulvenyl)ferrocene (**7a**). The structure of this compound was established using additionally ^{1}H NOE difference experiments and the 2D ^{1}H,^{13}C shift correlation spectrum. A NOE effect is observed from the methyl groups to H-2 as well as to H-5 in each ferrocene ring; this is probably caused by a rapid rotation of the pentafulvalene moieties vs the ferrocene system. However, no conclusions can be drawn on whether the configuration of **7a** is meso or dl (accidental spectroscopic isochronicities of a mixture of both excluded) since all attempts to separate these by chromatography using a chiral column phase (polytriacetylcellulose/ethanol) failed.

The 2-fold deprotonation of **7a** with ^{6}Li-enriched LiTMP in THF-d_8 yields a brown 0.1 M solution of the salt **8** which was studied by NMR spectroscopy. At room temperature, various signals in the ^{1}H and ^{13}C NMR spectra belonging to the ferrocene moiety and the vinyl groups show line-broadening effects which disappear when the sample is heated to 313 K. ^{1}H NOE difference spectra of **8** taken at this temperature prove that rapid rotation occurs around the bonds connecting the five-membered rings to the ethylene groups. Below the 273 K signal splitting is observed in the ^{1}H (Figure 1) and in the ^{13}C NMR spectra, pointing on

(1) (a) Becker, B.; Enkelmann, V.; Müllen, K. *Angew. Chem.* **1989**, *101*, 501–503; *Angew. Chem., Int. Ed. Engl.* **1989**, *28*, 458. (b) Gronert, S.; Streitwieser, A. *J. Am. Chem. Soc.* **1988**, *110*, 2836–2842. (c) O'Brien, D. H.; Russell, C. R.; Hart, A. J. *J. Am. Chem. Soc.* **1979**, *101*, 633–639. (d) Grutzner, J. B.; Lawlor, J. M.; Jackman, L. M. *J. Am. Chem. Soc.* **1972**, *94*, 2306–2315. (e) Johnels, D.; Edlund, U. *J. Am. Chem. Soc.* **1990**, *112*, 1647–1649. (f) Fraenkel, G.; Hallden-Abberton, M. P. *J. Am. Chem. Soc.* **1981**, *103*, 5657–5664. (g) Cox, R. H.; Terry, H. W. *J. Magn. Reson.* **1974**, *14*, 317–322.

(2) (a) Hoffmann, D.; Bauer, W.; Schleyer, P. v. R. *J. Chem. Soc., Chem. Commun.* **1990**, 208–211. (b) Bauer, W.; Clark, T.; Schleyer, P. v. R. *J. Am. Chem. Soc.* **1987**, *109*, 970–977.

(3) Paquette, L. A.; Bauer, W.; Sivik, M. R.; Bühl, M.; Feigel, M.; Schleyer, P. v. R. *J. Am. Chem. Soc.* **1990**, *112*, 8776–8789.

(4) Strohmeier, W.; Landsfeld, H.; Gernert, F. *Z. Elektrochem.* **1962**, *66*, 823–827.

(5) Eiermann, M.; Stowasser, K.; Hafner, K.; Bierwirth, K.; Frank, A.; Lerch, A.; Reusswig, J. *Chem. Ber.* **1990**, *123*, 1421–1431.

0002-7863/92/1514-135$03.00/0